Journal of Solid State Chemistry **151,** 210–219 (2000)
doi:10.1006/jssc.2000.8641, available online at http://www.idealibrary.com on IDEAL®

Two New Sr-Rich Layered Manganites with a 1:1 Bi–Sr Ordering: 1201 $Bi_{0.4}Sr_{2.6}MnO_{5-\delta}$ and 2201 $Bi_{0.9}Sr_{3.1}MnO_{6-\delta}$

D. Pelloquin, A. Maignan, M. Hervieu, C. Michel, and B. Raveau

Laboratoire CRISMAT, UMR 6508 associée au CNRS, ISMRA et Université de Caen, 6, Boulevard du Maréchal Juin, 14050 Caen Cedex, France

Received October 20, 1999; accepted January 26, 2000

Two new strontium-rich manganites with a layered structure, $Bi_{0.4}Sr_{2.6}MnO_{5-\delta}$ and $Bi_{0.9}Sr_{3.1}MnO_{6-\delta}$, have been synthesized and characterized, using X-ray powder diffraction and electron microscopy. The first, $Bi_{0.4}Sr_{2.6}MnO_{5-\delta}$, crystallizes in the space group *I4/mmm* with $a = 5.3756(1)$ Å and $c = 35.578(1)$ Å and shows for the first time the possibility to stabilize a manganite with a 1201-type structure. The second, $Bi_{0.9}Sr_{3.1}MnO_{6-\delta}$, which crystallizes in the $P2_1$ space group with $a = 5.2829(2)$ Å, $b = 5.2998(2)$ Å, $c = 23.9906(6)$ Å, and $\gamma = 90.27(2)^\circ$, exhibits a 2201 unmodulated structure. Both oxides are characterized by a 1:1 ordering between bismuth and strontium forming rows parallel to $\vec{b}$, while a quadrupling of the *c* parameter is observed in the case of the 1201 structure. The investigation of their magnetic properties shows a complex magnetic behavior connected to the existence of trivalent manganese in MnO_2 planes.

Key Words: **bismuth based manganites; layered structure; high resolution electron microscopy; Rietveld profile analysis.**

INTRODUCTION

Transition metal oxides with a layered structure have been shown to be particularly attractive for the generation of new physical properties such as superconductivity at high temperature in cuprates (see Refs. 1–3 for a review) or colossal magnetoresistance in the manganites (see Refs. 4 and 5 for a review). In this respect, bismuth-based systems are of great interest due to their ability to form intergrowths between distorded rock salt and perovskite layers, as illustrated by the superconductive cuprates $Bi_2Sr_2Ca_{m-1}Cu_mO_{2m+4}$ (6–9). In the case of manganese, a 2201-type phase $Bi_2Sr_2MnO_{6+\delta}$ (10), isotypic to $Bi_2Sr_2CuO_{6+\delta}$ (6), has also been synthesized. In fact, the stability of such oxides seems to be ensured by the presence of double bismuth–oxygen layers, which are at the origin of modulation phenomena in those structures (11, 12). Consequently, a sufficient bismuth content, corresponding to a Bi:Sr ratio close to 1, should be required for the generation of these materials. However, the recent discovery of a strontium-rich 2201 cobaltite $Bi_{1-x}Sr_{3+x}CoO_{6-\delta}$ (13) suggests that the latter condition does not need to be fulfilled for the synthesis of such intergrowths, provided the formation of carbonates can be avoided during the synthesis of these compounds.

On the basis of the above considerations, we have revisited the system Bi–Sr–Mn–O. We report herein on two new strontium-rich manganites with a layered structure derived from the perovskite. The first, $Bi_{0.4}Sr_{2.6}MnO_{5-\delta}$, is to date the only manganite which exhibits the 1201-type structure. The second, $Bi_{0.9}Sr_{3.1}MnO_{6-\delta}$, which exhibits the 2201-type structure, is isotypic to the corresponding cobaltite, being characterized like the latter by the absence of modulation, in contrast to $Bi_2Sr_2MnO_{6+\delta}$ (9) and to $Bi_2Sr_2CuO_{6+\delta}$ (6). Moreover, both oxides exhibit a quasi perfect 1:1 Bi–Sr ordering within their "bismuth strontium" rock salt layers.

CHEMICAL SYNTHESIS

The research on the 1201 phase in the Bi–Sr–Mn–O system was performed on the basis of the nominal compositions $Bi_{1-x}Sr_{2+x}MnO_{5-\delta}$, varying x from 0 to 1, for different δ values ranging from -0.5 to $+0.5$. In a similar way, the exploration of this system for the research on the 2201 phase was carried out for the nominal composition $Bi_{2-x}Sr_{2+x}MnO_{6-\delta}$, varying x from 0 to 1.5, for δ values ranging from -0.5 to $+0.5$.

Each sample was prepared in the absence of air, starting from the appropriate mixture of oxides Bi_2O_3, SrO, MnO_2, and Mn_2O_3. The presence of carbon dioxide or of carbonate must absolutely be avoided. It leads indeed to the formation of oxycarbonates which destabilize the 1201 and 2201 manganites; this probably explains why these compounds have never been synthesized to date. Thus, each operation was carried out in a drybox. To avoid contamination by CO_2, SrO was initially prepared by decomposing SrO_2 or $Sr(OH)_2 \cdot 8H_2O$ at 1100°C and stored in a drybox. Then the appropriate amounts of SrO, Bi_2O_3, MnO_2, and Mn_2O_3 were mixed in a drybox, placed in a sealed evacuated silica tube, heated to a temperature ranging from 900 to

0022-4596/00 $35.00

1000°C at 150°C h^{-1}, kept at this temperature for 24 h, and finally quenched to room temperature.

For these experimental compositions, two nearly monophasic samples were synthesized for the nominal compositions $Bi_{0.4}Sr_{2.6}MnO_{4.9}$ ($x = 0.6$, $\delta = 0.1$) and $BiSr_3MnO_6$ ($x = 1$, $\delta = 0$), respectively.

STRUCTURAL AND MAGNETIC CHARACTERIZATIONS

The electron diffraction (ED) studies were carried out using a JEOL 200 CX microscope fitted with an eucentric goniometer ($\pm 60°$) while the high-resolution electron microscopy (HREM) images were obtained with a TOPCON 02B microscope operating at 200 kV and having a point resolution of 1.8 Å. HREM image calculations were carried out with the Mac-Tempas multislice program. Both microscopes are equipped with an EDX analyzer.

X-ray powder diffraction (XRPD) patterns were collected using a Philips vertical diffractometer equipped with a secondary graphite monochromator and working with Cu$K\alpha$ radiation. Data were collected by step scanning over an angular range $5° \leq 2\theta \leq 110°$ and next were treated by profile analysis with the program Fullprof (version 3.2) (14).

Magnetic susceptibility $\chi(T)$ measurements were investigated at low temperature (5–400 K) using an AC–DC SQUID Quantum Design magnetometer (ZFC method) and at high temperature (300–800 K) using the Faraday method with, in both cases, an applied field of 3 kG. Resistivity measurements were recorded with a physical properties measurements system (PPMS) from Quantum Design (four-probe method).

1. *The 1201 Manganite $Bi_{0.4}Sr_{2.6}MnO_{5-\delta}$*

The XRPD pattern of this phase (Fig. 1) shows that it is closely related to the 1201 structure observed for $Tl_{0.5}Pb_{0.5}Sr_2CuO_5$ (15). The EDS analysis performed in numerous microcrystallites confirms the cationic composition $Bi_{0.4}Sr_{2.6}Mn$, whereas the chemical analysis, using redox titration, leads to an actual oxygen content close to 4.7, i.e., $\delta = 0.3$.

The [001], [1$\bar{1}$0], and [100] ED patterns (Fig. 2) show a system of intense reflections characteristic of the 1201-type structure, i.e., corresponding to the cell parameters $a = b \approx a_p \approx 3.8$ Å and $c \approx 8.9$ Å. Nevertheless, the reconstruction of the reciprocal space by tilting around the crystallographic axes evidences extra reflections, corresponding to a tetragonal supercell with $a = b \approx a_p\sqrt{2}$ and $c \approx 4c_{1201} \approx 35.5$ Å. The reflection conditions hkl: $h + k + l = 2n$ are compatible with the space group $I4/mmm$. Consequently, the XRPD pattern of this phase can be indexed in a tetragonal cell with the following parameters:

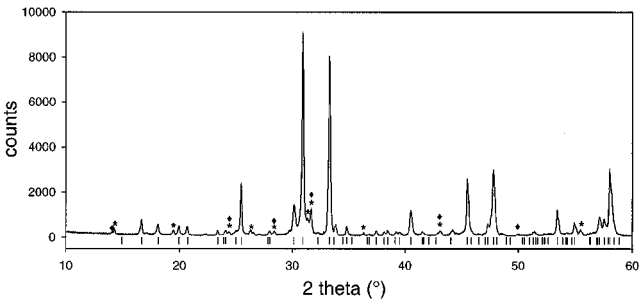

FIG. 1. Part of the experimental X-ray pattern recorded for $Bi_{0.4}Sr_{2.6}MnO_{5-\delta}$, indexed (verticals bars) in a tetragonal cell ($a = 5.3756(1)$ Å and $c = 35.578(1)$ Å, $I4/mmm$). Peaks with stars and black diamonds correspond to $Sr(OH)_2 \cdot 2H_2O$ and Sr_2MnO_4 phases, respectively.

$$a = 5.3756(1) \text{ Å} \quad \text{and} \quad c = 35.578(1) \text{ Å}.$$

In order to confirm the layer stacking mode of this new manganite and to determine the origin of the superstructure, an HREM study was carried out. The best orientation to image the layer stacking is the $[100]_p$, i.e., the $[\bar{1}10]$ orientation of the supercell. A typical image is given in Fig. 3, where the cation positions are correlated to the dark dots (close to the Scherzer value). The contrast is very similar to the one recorded in the 1201-type cuprates (16). One observes easily a group of three adjacent rows of staggered dark dots (arrows), 3.8 Å spaced along [110] and 2.5 Å along [001]. This contrast is characteristic of rock salt-type $[AO]_\infty$ layers. These triple rows are separated along c by a single row of smaller dots which is associated with one $[MnO_2]_\infty$ layer. Such a regular stacking mode leads to a periodicity close to 8.9 Å along the c axis that, correlated to the actual composition $Bi_{0.4}Sr_{2.6}MnO_x$, can be described by following sequence –[SrO]–[(Sr,Bi)O]–[SrO]–[MnO_2]–, which confirms the 1201 type of the structure. The theoretical images calculated with the positional parameters refined from XRPD data (see further) confirm this hypothesis; the calculated image for a crystal thickness of 25 Å and a focus value close to -30 nm is given in Fig. 3b. However, the contrast along this direction does not explain the quadrupling of the c parameter, evidenced from the ED patterns. In fact, the quadrupling of c can easily be explained from the $[110]_p$ HREM images (Fig. 4a), where high electronic density zones are imaged as bright dots. On the edge of the crystal one can identify triple rows of bright dots, running along $\vec{a}$, and separated by single rows of gray dots long $\vec{c}$, which correspond to triple $[AO]_\infty$ layers and a single $[MnO_2]_\infty$ layer, respectively. Along $\vec{a}$, the bright spots are spaced by 2.7 Å, but in the thicker zone the periodicity of the contrast is in fact 5.4 Å at the level of the intermediate $[AO]_\infty$ layer (see enlargement on Fig. 4, where one bright

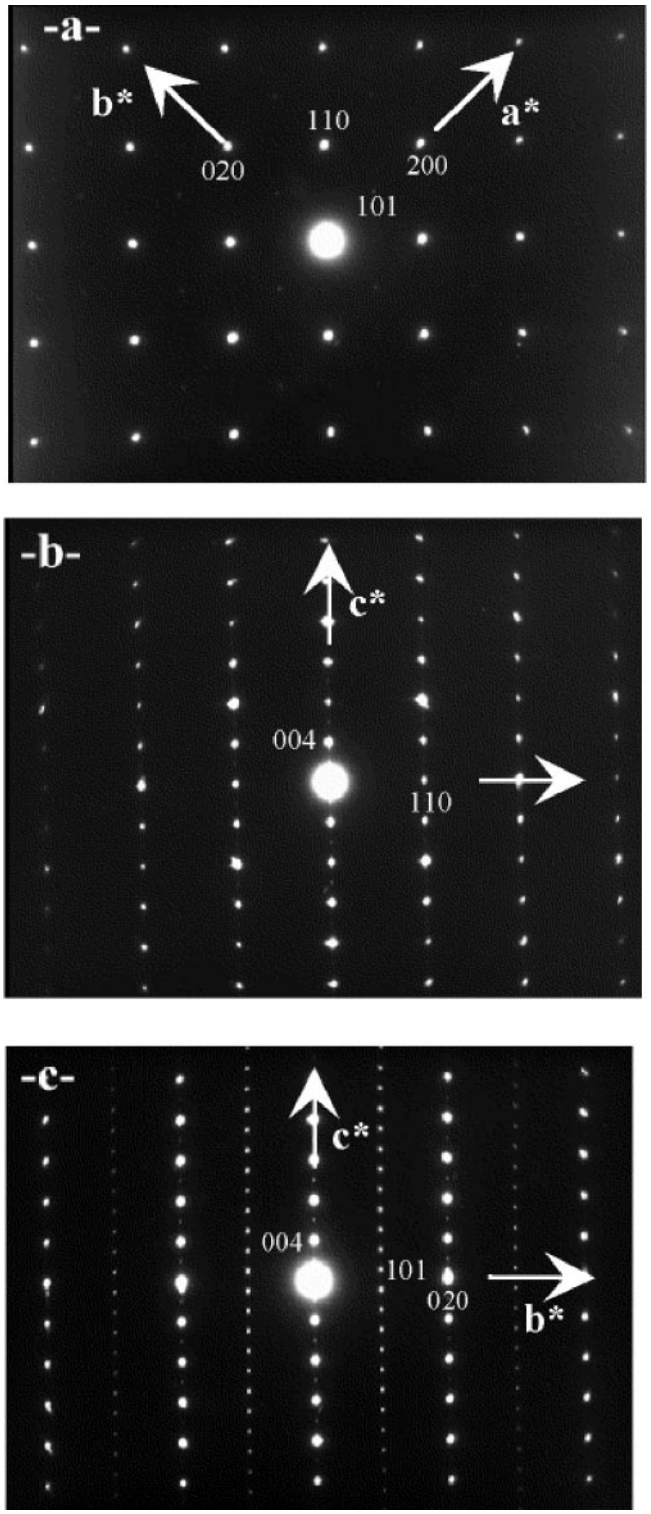

FIG. 2. Experimental ED patterns, oriented (a) [001], (b) [1$\bar{1}$0], and (c) [100], indexed in the unit cell $a_p\sqrt{2} \times a_p\sqrt{2} \times 4c_{1201}$.

dot alternates with one gray dot in the intermediate $[AO]_\infty$ layer). This suggests that in this intermediate $[AO]_\infty$ layer one [010] row out of two is preferentially occupied by

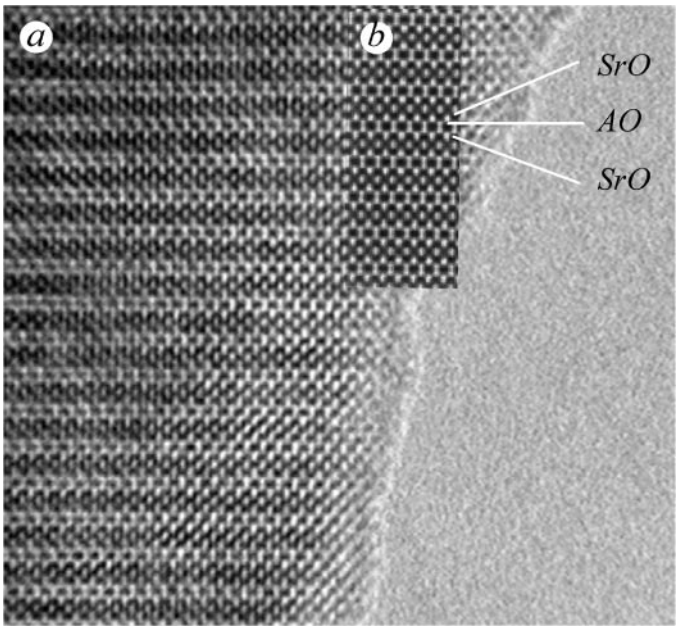

FIG. 3. (a) Experimental and (b) calculated HREM image recorded along the [1$\bar{1}$0] direction. Black dots (arrows) are correlated to Bi and Sr atoms.

bismuth, the other one being occupied by strontium. Thus the ideal composition of this intermediate layer should be $[Bi_{0.5}Sr_{0.5}O]_\infty$ and the 1 : 1 ordering between bismuth and strontium within this layer would correspond to the sequence Bi–Sr–Bi along $\vec{a}$. Each ordered layer is then sandwiched between two $[SrO]_\infty$ layers according to the formulation $[SrO][Bi_{0.5}Sr_{0.5}O][SrO]$, corresponding to the triple $[AO]$ layer. The quadrupling of the c parameter, clearly seen from the enlargement of Fig. 4, is then easily

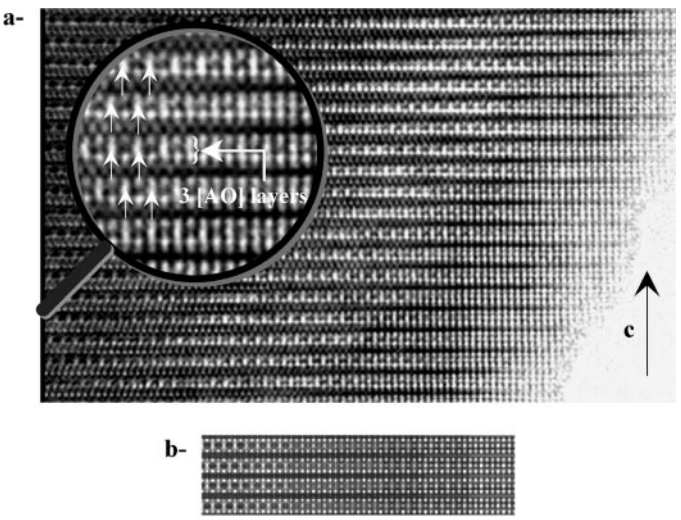

FIG. 4. (a) Experimental and (b) calculated HREM images recorded along the [010] (or [100]) direction. Brights dots are correlated to Bi and Sr atoms.

explained by the stacking of the ordered $[Bi_{0.5}Sr_{0.5}O]_\infty$ layers along $\vec{c}$: two successive BiSr layers out of four are shifted by $a/2$ with respect to each other leading to the sequence described in Fig. 5.

Thus, a structural model (Fig. 6) can be proposed, according to the ideal formula $(Bi_{0.5}Sr_{0.5})Sr_2MnO_5$, which corresponds to the intergrowth of single perovskite layers $[SrMnO_3]_\infty$ with ordered rock salt layers $[(SrO)(Bi_{0.5}Sr_{0.5}O)]$. In fact the actual composition is slightly different from the ideal one, suggesting a partial disordering at the level of the BiSr layers (bismuth deficiency), as well as an oxygen deficiency.

In order to check this structural model, and especially to be able to perform HREM simulations, structure calculations were carried out from XRPD data in the *I*4/*mmm* space group. Due to the too great number of variable parameters (14 independent atoms), a unique *B* value was applied to each kind of atoms, and constraints were fixed for some oxygens. Refinements of the structure were carried out starting from the parameters of the 1201 structure and taking into consideration the ordering phenomena observed by HREM. Sr_2MnO_4 and $Sr(OH)_2nH_2O$ detected as impurities from TEM and XRPD data were introduced as secondary phases. Further to intermediate calculations, oxygen vacancies ($\delta \approx 0.2$) were statistically distributed at the level of the SrO and MnO_2 layers, i.e., O(3) and O(1), respectively. The final agreement factors $R_p = 10.7\%$, $R_{wp} = 13.7\%$, $R_i = 6.7\%$, and $\chi^2 = 5.04$ were obtained for the structural parameters listed in Table 1. Although these results cannot be considered as accurate, they confirm the HREM observations. Note that the refinement of the cationic composition shows that the Bi site is partially occupied by strontium, leading to the formula $Bi_{0.42}Sr_{2.58}MnO_{5-\delta}$ in good agreement with the EDS results. Thus, the BiSr ordering in the oxide can better be described by the alternation of BiSr rows (84% Bi) with Sr rows. More importantly, these data allow the HREM contrast to be simulated (Fig. 4b). For a focus value of -65 nm, with a crystal thickness ranging from 5.5 to 44 Å, one observes that this contrast fits perfectly with the experimental one.

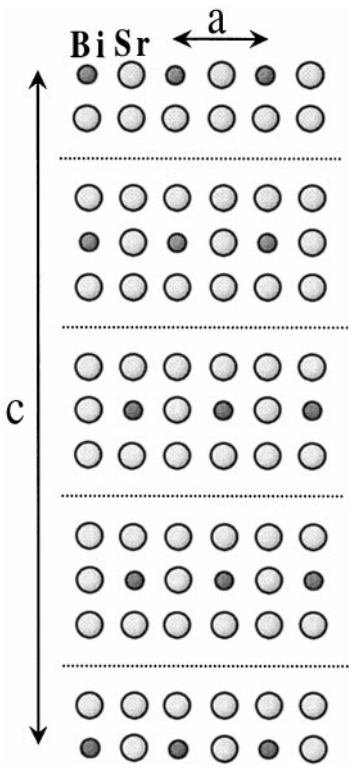

FIG. 5. Stacking of the Bi–Sr and Sr layers along the *c* axis in the ordered 1201 oxide $Bi_{0.4}Sr_{2.6}MnO_{5-\delta}$. For simplicity, oxygen atoms are not drawn.

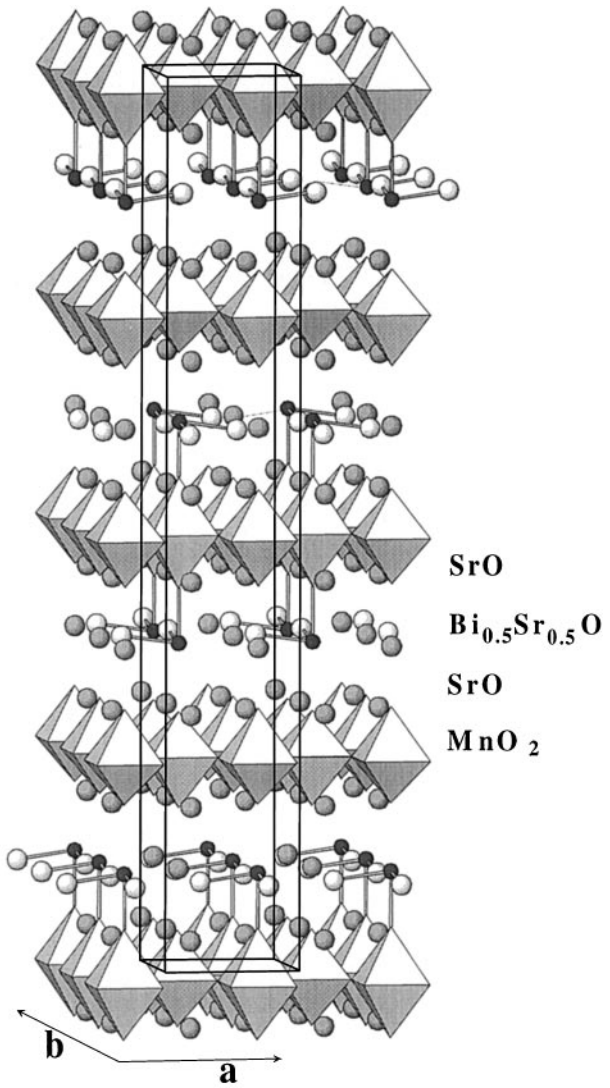

FIG. 6. Perpective view of the structure of the 1201 manganite. The stacking layers and the Bi–O bonds are evidenced.

TABLE 1
Refined Variable Structural Parameters and Main Interatomic Distances for $Bi_{0.4}Sr_{2.6}MnO_{5-\delta}$

Atom	Site	x	y	z	B (Å^2)	n	Distances (Å)		
Bi	4*e*	0.0	0.0	0.6256(2)	1.0(1)	3.32(4)	Mn(1)–O(1)	1.901(1)	×4
Sr	4*e*	0.0	0.0	0.6256(2)	1.0(1)	0.68(4)	–O(3)	1.89(5)	×2
Sr(1)	4*e*	0.0	0.0	0.1262(3)	0.09(4)	4	Mn(2)–O(1)	1.901(1)	×4
Sr(2)	8*g*	0.5	0.0	0.0499(2)	0.09(4)	8	–O(4)	2.19(4)	×2
Sr(3)	8*g*	0.5	0.0	0.1989(2)	0.09(4)	8	Mn(3)–O(2)	1.901(1)	×4
Mn(1)	2*a*	0.0	0.0	0.0	0.3(1)	2	–O(6)	1.87(4)	×1
Mn(2)	2*b*	0.0	0.0	0.5	0.3(1)	2	–O(7)	1.85(4)	×1
Mn(3)	4*e*	0.0	0.0	0.25	0.3(1)	4	Bi/Sr–O(4)	2.28(4)	×1
O(1)	8*h*	0.25[a]	0.25[a]	0.0	0.8[a]	7.4(3)	–O(5)	2.36(3)	×2
O(2)	8*e*	0.25	0.25	0.25	0.8[a]	8[b]	–O(6)	2.56(4)	×1
O(3)	4*e*	0.0	0.0	0.053(1)	0.8[a]	3.2(2)	Sr(1)–O(3)	2.60(1)	×1
O(4)	4*e*	0.0	0.0	0.561(1)	0.8[a]	4[b]	–O(5)	2.736(5)	×4
O(5)	16*n*	0.0	0.566(5)	0.6365(7)	0.8[a]	8[b]	–O(7)	2.55(4)	×1
O(6)	4*e*	0.0	0.0	0.302(1)	0.8[a]	4[b]	Sr(2)–O(1)	2.602(5)	×4
O(7)	4*e*	0.0	0.0	0.198(1)	0.8[a]	4[b]	–O(3)	2.690(3)	×2
							–O(4)	2.720(6)	×2
			Space group *I*4/*mmm*				–O(5)	3.10(3)	×1
			$a = 5.3756(1)$ Å, $c = 35.578(1)$ Å				Sr(3)–O(2)	2.630(5)	×4
			$R_p = 10.7\%$, $R_B = 6.7\%$, $\chi^2 = 5.04$				–O(5)	2.40(3)	×1
							–O(6)	2.690(1)	×2
							–O(7)	2.690(1)	×2

[a] Parameter not refined.
[b] Fixed value since e.s.d.'s value is greater than the deviation.

The interatomic distances (Table 1) show different distortions of the MnO_6 octahedra depending on the nature of the A atom (Sr or Bi) linked to their apical oxygen. The bismuth cation exhibits three shorter Bi–O bonds, suggesting some stereoactivity of its lone pair. A complete neutron diffraction study of this phase will be necessary for further discussion.

Finally, it is worth pointing out that only a few extended defects have been observed during the HREM study of this 1201 manganite. A first type consists of the local disappearance along $\vec{c}$ of the mixed ordered intermediate layer, forming only a double $[SrO]_\infty$ layer instead of a triple one in the perfect structure. It locally forms a defective 0201 member, Sr_2MnO_4, as illustrated in Fig. 7a (black arrow). The second type of defect (white bracket in Fig. 7b) corresponds to deviations from the Bi–Sr ordering along $\vec{c}$, involving a local breaking of the fourfold periodicity.

2. *The 2201 Manganite $Bi_{0.9}Sr_{3.1}MnO_{6-\delta}$*

The EDS analysis performed on more than 15 microcrystals leads to the cationic composition $Bi_{0.86}Sr_{3.08}Mn$, close to the nominal one. The chemical analysis using redox titration allows the oxygen content to be determined, leading to the formula $Bi_{0.9}Sr_{3.1}MnO_{5.9}$ involving only Mn(III). The analysis of the [*hk*0] ED patterns (Fig. 8) and the reconstruction of the reciprocal space show that this phase exhibits close relationships with the 2201 structure previously observed for $Bi_2Sr_2MnO_{6+\delta}$ (10) and for $Bi_{1-x}Sr_{3+x}CoO_{6-\delta}$ (13), indicating the following parameters: $a \approx b \approx a_p\sqrt{2}$, and $c \approx 24$ Å. In fact the oxides $Bi_{0.9}Sr_{3.1}MnO_{5.9}$ and $Bi_{1-x}Sr_{3+x}CoO_{6-\delta}$ exhibit significant structural differences with respect to $Bi_2Sr_2MnO_{6+\delta}$: first they are characterized by a monoclinic symmetry instead of orthorhombic and second their ED patterns do not show any incommensurate extra reflection associated with the 0*k*0 reflections. Like the cobaltite, $Bi_{0.9}Sr_{3.1}MnO_{5.9}$ exhibits additional streaks along $\vec{c}$, but in contrast to the latter this phenomenon appears on the two [010] and [100] patterns (see white arrow in Fig. 8c) instead of only on the [010] orientation. This observation suggests the existence of much more important disordering, compared to the cobaltite.

The reflection conditions 00*l*, $l = 2n$ obtained from the ED patterns lead to the $P2_1$ space group and the XRPD patterns (Fig. 9) can be indexed on a monoclinic cell with the parameters.

$$a = 5.2829(2)\text{ Å}, \quad b = 5.2998(2)\text{ Å}, \quad c = 23.9906(6)\text{ Å},$$
$$\gamma = 90.27(2)^\circ,$$

indicating a contraction in the (001) plane and an expansion along $\vec{c}$ with respect to $Bi_2Sr_2MnO_{6+\delta}$, whose

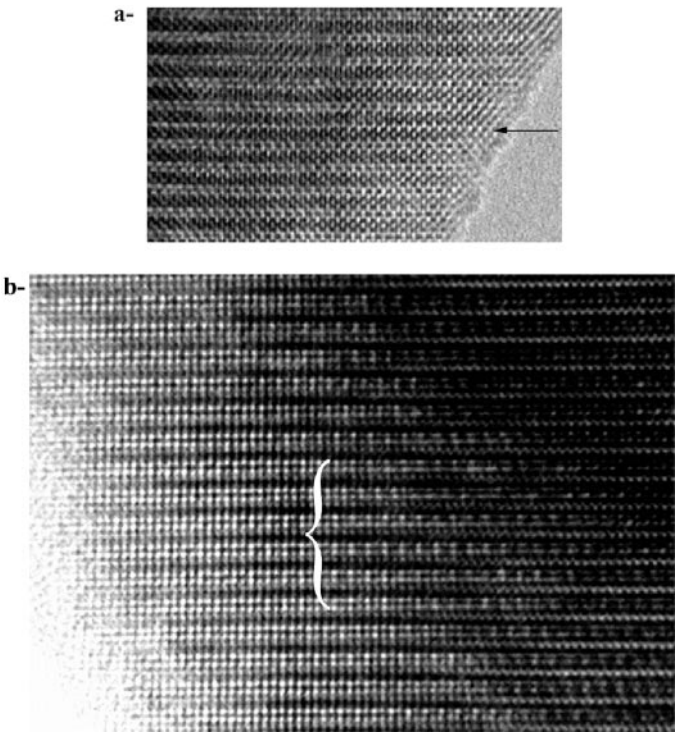

FIG. 7. Extended defects observed from HREM images (a) leading to a defective 0201 member (black arrow) or (b) involving a local breaking (white bracket) of the fourfold periodicity.

orthorhombic cell exhibits the following parameters: $a = 5.451(2)$ Å, $b = 5.426(2)$ Å, and $c = 23.6135(8)$ Å (10).

The close relationships with the cobaltite $Bi_{1-x}Sr_{3+x}Co_{6-\delta}$ (13) allow a similar structural model to be proposed (Fig. 10). In this model, single perovskite $[SrMnO_3]_\infty$ layers are intergrown with triple rock salt $[Bi_{0.9}Sr_{3.1}O_3]_\infty$ layers. Within the rock salt layers two mixed layers $[Bi_{0.45}Sr_{0.55}O]_\infty$ are sandwiched between two $[SrO]_\infty$ layers and, within each mixed layer, one [010] bismuth row (90% Bi + 10% Sr) alternates with one strontium row along $\vec{a}$ so that along this direction one double bismuth ribbon alternates with one double strontium row, as shown in Fig. 10b. In contrast, the view of the structure along [100] (Fig. 10a) shows that the [100] bismuth and strontium rows adopt a staggered configuration respectively, two successive $[Bi_{0.45}Sr_{0.55}O]_\infty$ (001) layers being shifted by $\vec{b}/2$ with respect to each other.

Structure calculations were performed, using the XRPD data, in the space group $P2_1$ in order to check this model. Bismuth sites were assumed to be 10% occupied by strontium. Due to the large number of independent atoms (22), a same B factor was attributed to identical atoms, and constraints were applied to the x and y parameters of most of the atoms which were fixed to their theoretical values, without any refinement. For these atomic coordinates (Table 2), the following agreement factors were obtained: $R_p = 9.3\%$, $R_{wp} = 13.0\%$, $R_i = 6.6\%$, and $\chi^2 = 5.1$. These results confirm that $Bi_{0.9}Sr_{3.1}MnO_{5.9}$ exhibits the 2201-type structure with the same Bi–Sr ordering previously observed for the cobaltite $Bi_{1-x}Sr_{3+x}CoO_6$ (13). The poor accuracy on the atomic positions does not allow any discussion about the interatomic distances which are in any

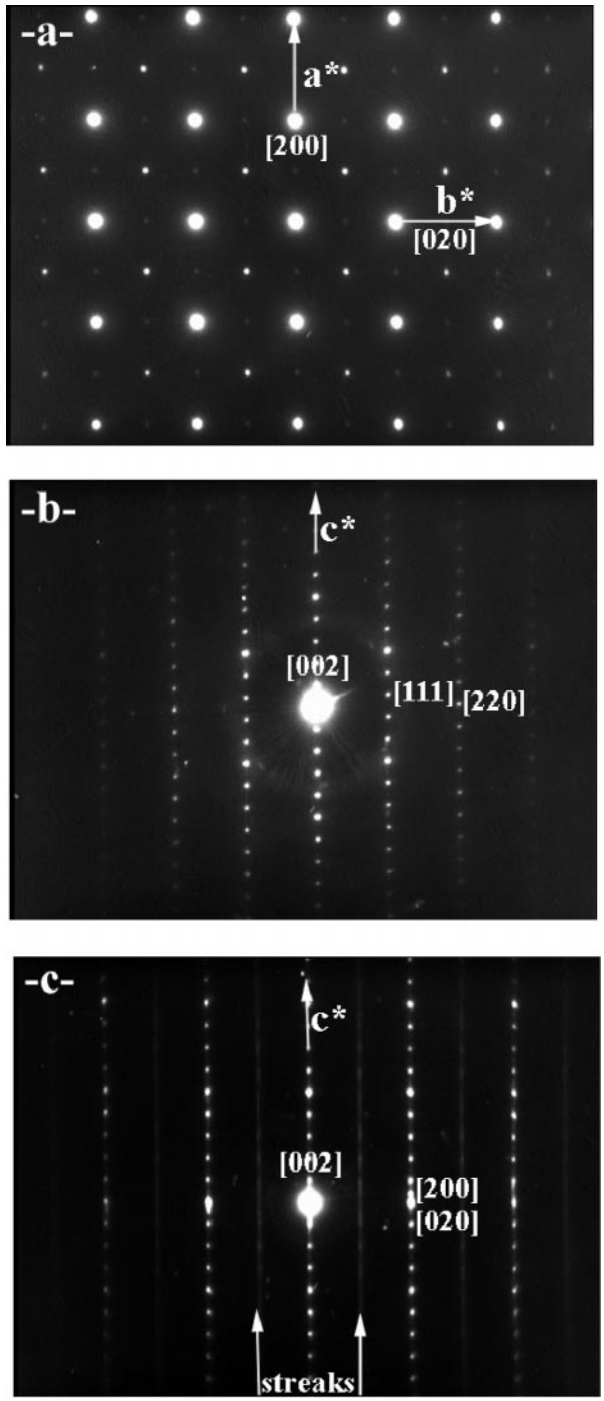

FIG. 8. Experimental ED patterns, oriented (a) [001], (b) [1$\bar{1}$0], and (c) [100], indexed in the unit cell $a_p\sqrt{2} \times a_p\sqrt{2} \times c_{2201}$.

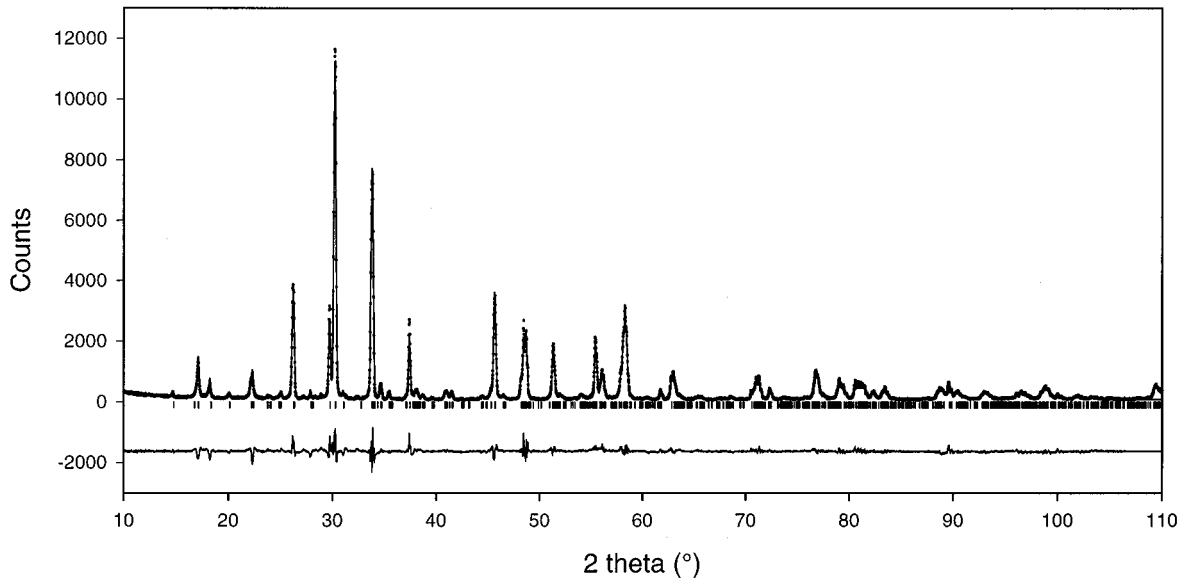

FIG. 9. Experimental (crosses), calculated, and difference (solid lines) powder X-ray diffraction patterns of the 2201-type phase $Bi_{0.9}Sr_{3.1}MnO_{5.9}$. Verticals bars indicate the Bragg angle positions calculated from the $P2_1$ space group.

case close to those previously observed for this type of compounds.

In fact, such a structural model does not explain the streaks observed on the [100] and [010] ED patterns. The corresponding simulated ED patterns are significantly different for the [100] view (inset Fig. 10a) than for the [010] one (inset Fig. 10b). Thus the different streaks correspond to the superposition of these two kinds of patterns. This observation can be explained as follows: the 1:1 Bi–Sr ordering is identical in each $[Bi_{0.9}Sr_{1.1}O_2]_\infty$ (001) double layer, exactly as described above, but along $\vec{c}$ two successive double layers can be rotated by 90° with respect to each other, so that the two configurations of the structure described for the [100] and [010] orientations (Fig. 10) may appear for a same [100] or [010] orientation. The [100] HREM images (Fig. 11) of this phase confirm this viewpoint. Rows of sticks corresponding to the double Bi ribbons ([010] configuration of the BiSr layers in Fig. 10a) are indeed randomly stacked with rows of staggered dots ([100] configuration of the Bi–Sr layers on Fig. 10a) along $\vec{c}$.

3. *Magnetic and Transport Properties*

These new layered manganites, namely $Bi_{0.4}Sr_{2.6}MnO_{4.7}$ and $Bi_{0.9}Sr_{3.1}MnO_{5.9}$, are characterized by high room temperature resistivity values, as illustrated in Fig. 12 in the case of Bi-1201 manganite, with $\rho_{300K} \approx 2.3\,10^3\,\Omega$.cm and $\rho_{300K} > 10^6\,\Omega$.cm for the strontium-rich Bi-1201 and Bi-2201, respectively. This behavior ($\rho_{300K} > 10^3\,\Omega$.cm) is expected if one considers the nearly trivalent oxidation state of manganese in these phases; i.e., the lack of a sufficient amount of mixed valency prevents the charge delocalization as for the $LaMnO_3$ insulating perovskite (17).

In order to check the Mn oxidation state—Mn^{3+} ($3d^4$) in oxides exhibits usually a high spin $t_{2g}^3 e_g^1$ state—magnetic susceptibility $\chi(T)$ measurements at 3 kG have been performed for temperatures in the ranges 5 to 400 K (SQUID) and 100 to 600 K (Faraday method). The field was applied after a zero-field cooling process. The corresponding data are given in Fig. 13 for the strontium-rich Bi-1201, namely $Bi_{0.4}Sr_{2.6}MnO_{4.7}$, and Bi-2201, namely $Bi_{0.9}Sr_{3.1}MnO_{5.9}$, and compared with the $\chi(T)$ data collected for the stoichiometric $Bi_2Sr_2MnO_{6+\delta}$ compound synthesized by the same experimental process as that used for the two former compounds. The $\chi(T)$ curves exhibit very different shapes with a very narrow paramagnetic region for $Bi_{0.9}Sr_{3.1}MnO_{5.9}$ as shown in Fig. 13 (inset). Consequently, no significant fitting of the paramagnetic region has been possible for the latter compound. The fittings performed in the temperature range 250 to 600 K with the Curie–Weiss law $\chi = C/(T - \theta_p)$, where C and θ_p are the Curie constant and paramagnetic temperature, respectively, yield the following effective moments μ_{eff} per manganese and paramagnetic temperatures θ_p:

$\mu_{eff} = 5.1(1)\mu_B$ and $\theta_p = -49$ K for the stoichiometric Bi-2201, namely $Bi_2Sr_2MnO_{6+\delta}$

$\mu_{eff} = 5.3(1)\mu_B$ and $\theta_p = -261$ K for the strontium-rich Bi-1201, namely $Bi_{0.4}Sr_{2.6}MnO_{4.7}$.

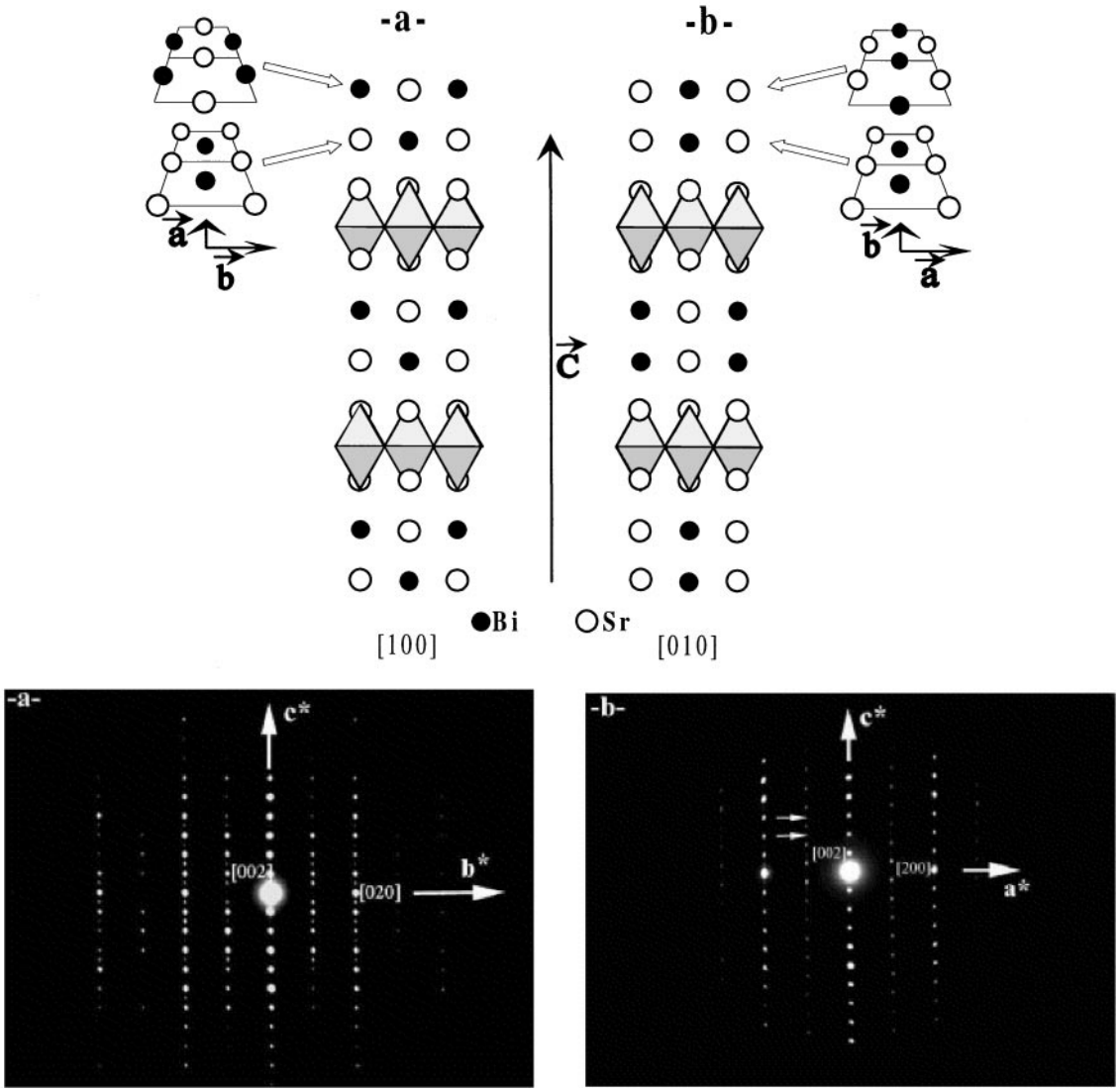

FIG. 10. Projection along (a) [100] and (b) [010] directions of the structure of the 2201 manganite with the ideal composition $BiSr_3MnO_6$ and corresponding ED patterns. Perspective views of the Bi–Sr layers in the $(\vec{a}, \vec{b})$ plane are also shown.

These values are close to those previously observed in the stoichiometric 2201 $Bi_2Sr_2MnO_{6+\delta}$ ($\mu_{eff} = 4.96\ \mu_B$ and $\theta_p = -41$ K) (10). The μ_{eff} values are also in agreement with those reported for $Sr_5Mn_4CO_{13}$ ($\mu_{eff} = 5.09\ \mu_B$) (18) and $Bi_{3.6}Sr_{12.4}Mn_8O_{28+\delta}$ ($\mu_{eff} = 4.7\ \mu_B$) (19). All these μ_{eff} values are consistent with that expected for high-spin Mn(3+) ($\mu_{eff} = 4.9\ \mu_B$) and thus in good agreement with the charge balance calculations obtained from the actual compositions, $Bi_{0.4}Sr_{2.6}MnO_{4.7}$ and $Bi_2Sr_2MnO_{6.5}$. The negative θ_p values are indicative of the antiferromagnetic interactions in these compounds, stronger in Bi-1201 than in Bi-2201.

However, comparison of the three $\chi(T)$ curves for temperatures smaller than that of the paramagnetic region reveals large differences for these Bi-based manganites. In particular, the magnitude of the susceptibility peak observed for the stoichiometric Bi-2201 at 140 K (curve a in Fig. 13), which is in good agreement with Ref. (10), is more likely a small bump on the $\chi(T)$ curve of $Bi_{0.4}Sr_{2.6}MnO_{4.7}$ (curve b in Fig 13) and is hardly visible for $Bi_{0.9}Sr_{3.1}MnO_{5.9}$ (curve c in Fig. 13). The higher values of the susceptibility for Bi-2201 have been previously ascribed to ferrimagnetism which is a result of the modulated structure of this phase (10). Its magnetic structure established from the neutron diffraction data shows that the Mn^{3+} spins are parallel to the *c*-axis, i.e., perpendicular to the MnO_2 planes of this highly anisotropic structure, and that the different crystallographic sites in the manganese layers, resulting from

TABLE 2
Refined Variable Structural Parameters for $Bi_{0.9}Sr_{3.1}MnO_{6-\delta}$

Atom	Site	x	y	z	B (Å^2)
Bi(1)	2*a*	0.75[a]	0.5[a]	0.5517(26)	0.2(3)
Bi(2)	2*a*	0.75[a]	0.0[a]	0.4335(26)	0.2(3)
Sr(1)	2*a*	0.25[a]	0.5[a]	0.3185(27)	0.09(4)
Sr(2)	2*a*	0.25[a]	0.0[a]	0.6644(27)	0.09(4)
Sr(3)	2*a*	0.25[a]	0.5[a]	0.1623(27)	0.09(4)
Sr(4)	2*a*	0.25[a]	0.0[a]	0.8209(27)	0.09(4)
Sr(5)	2*a*	0.25[a]	0.0[a]	0.4371(32)	0.09(4)
Sr(6)	2*a*	0.25[a]	0.5[a]	0.5507(32)	0.09(4)
Mn(1)	2*a*	0.25[a]	0.0[a]	0.25	0.4(1)
Mn(2)	2*a*	0.25[a]	0.5[a]	0.75	0.4(1)
O(1)	2*a*	0.0[a]	0.25[a]	0.25[a]	0.8(2)
O(2)	2*a*	0.5[a]	0.25[a]	0.25[a]	0.8(2)
O(3)	2*a*	0.0[a]	0.75[a]	0.25[a]	0.8(2)
O(4)	2*a*	0.5[a]	0.75[a]	0.25[a]	0.8(2)
O(5)	2*a*	0.25[a]	0.0[a]	0.3419(12)	0.8(2)
O(6)	2*a*	0.25[a]	0.5[a]	0.6581(12)	0.8(2)
O(7)	2*a*	0.25[a]	0.0[a]	0.1481(12)	0.8(2)
O(8)	2*a*	0.25[a]	0.5[a]	0.8519(12)	0.8(2)
O(9)	2*a*	0.339(5)	0.5[a]	0.4373(18)	0.8(2)
O(10)	2*a*	0.161(5)	0.0[a]	0.5627(18)	0.8(2)
O(11)	2*a*	0.75[a]	0.939(6)	0.4429(16)	0.8(2)
O(12)	2*a*	0.75[a]	0.561(6)	0.5571(16)	0.8(2)

Space group $P2_1$
$a = 5.2829(2)$ Å, $b = 5.2998(2)$ Å, $c = 23.9906(6)$ Å, $\gamma = 90°27(2)$
$R_p = 9.3\%$, $R_B = 6.6\%$, $\chi^2 = 5.1$

[a] Parameters not refined.

Constraints: $x_{O(9)} + x_{O(10)} = 0.5$; $y_{O(11)} + y_{O(12)} = 1.5$, and for $i = 5, 7, 9$, and 11, $z_{O(i)} + z_{O(i+1)} = 1$.

modulated structure, forbid a complete antiferromagnetic order of the Mn cations in the plane to occur, leading to ferrimagnetism. Although the 1201 and 2201 strontium-rich

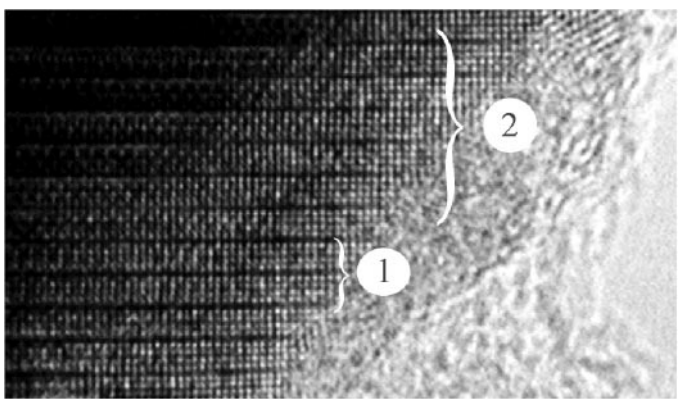

FIG. 11. Experimental HREM image recorded along [100]-type orientations showing the aleatory distribution (white brackets) of two configurations (see Fig. 10): (1) aligned successive Bi rows and (2) staggered successive Bi rows. Bright dots in the thin edge of the crystal are correlated to Bi and Sr atoms.

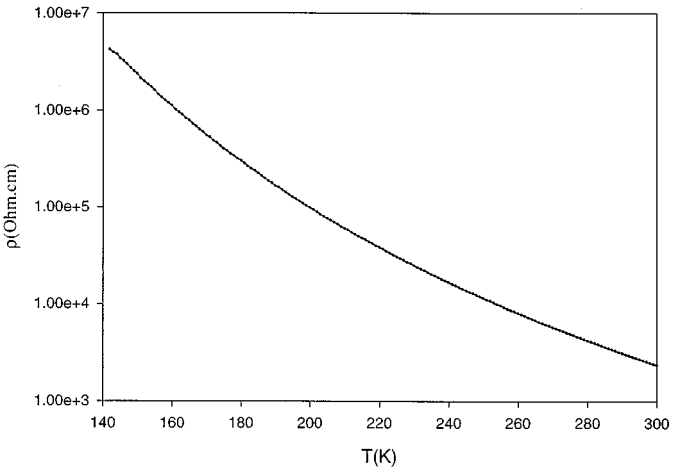

FIG. 12. $\rho = f(T)$ curve recorded for Bi-1201, namely $Bi_{0.4}Sr_{2.6}MnO_{5-\delta}$.

phases exhibit unmodulated structures, several Mn crystallographic sites are still observed (Tables 1 and 2). Nevertheless, the magnetic behavior is highly different for $Bi_{0.9}Sr_{3.1}MnO_{5.9}$ (inset in Fig. 13) which exhibits an extended maximum around 350 K with a progressive χ decrease starting from this temperature down to 100 K. Such a curve shape is reminiscent of 2D antiferromagnets such as Sr_2MnO_4 (20) for which the layered structure is thought to be at the origin of the strong antiferromagnetic fluctuations already observed 100 K above T_N. Similarly, such magnetic fluctuations are responsible for the χ decrease below 350 K in the case of $Bi_{0.9}Sr_{3.1}MnO_{5.9}$ but T_N is probably well below that temperature. However, the unmodulated 1201-type $Bi_{0.4}Sr_{2.6}MnO_{4.7}$ phase (curve b in Fig. 13) exhibits an intermediate behavior between these 2201 phases. The existence of a small oxygen deficiency in this compound generates several kinds of MnO_x polyhedra. Accordingly, a perfect antiferromagnetic ordering in the planes is probably more difficult to establish and so a small susceptibility peak is observed.

CONCLUDING REMARKS

This study shows for the first time the possibility to generate layered manganites with a low Bi : Sr ratio, and demonstrates that the experimental conditions play an important role in the synthesis of the oxides. $Bi_{0.4}Sr_{2.6}MnO_{5-\delta}$ represents the first 1201 manganite which has been synthesized to date, whereas $Bi_{0.9}Sr_{3.1}MnO_{6-\delta}$ exhibits, like $Bi_2Sr_2MnO_{6+\delta}$, a 2201 structure but differs from the latter by the absence of modulations. The common structural feature to these two new manganites concerns the 1 : 1 Bi–Sr ordering, forming rows running along *b*; this behavior may be related to the particular stereoactivity of the $6s^2$ lone

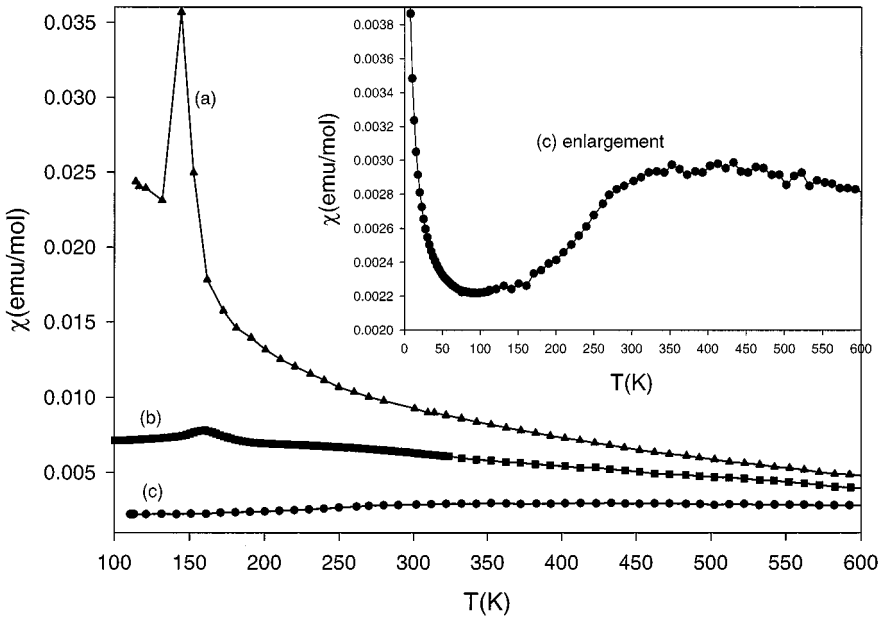

FIG. 13. Temperature dependence of the molar magnetic susceptibility $\chi(T)$ recorded for (a) stoichiometric Bi-2201, namely $Bi_2Sr_2MnO_{6+\delta}$, (b) Bi-1201, namely $Bi_{0.4}Sr_{2.6}MnO_{5-\delta}$, and (c) strontium-rich Bi-2201, namely $Bi_{0.9}Sr_{3.1}MnO_{5.9}$. In the inset the curve c is enlarged.

pair of Bi^{3+}, avoiding in this way the modulation of the structure encountered in the bismuth-rich 2201 manganite. A neutron diffraction study will be necessary to understand the relationship between structure and magnetism in these oxides.

ACKNOWLEDGMENTS

The authors are grateful to Dr. N. Nguyen for susceptibility measurements at high temperature.

REFERENCES

1. J. G. Bednorz and K. A. Muller, *Z. Phys. B* **64,** 189 (1986).
2. B. Raveau, C. Michel, M. Hervieu, and D. Groult, *in* "Crystal Chemistry of High Tc Superconductive cuprates," Springer Verlag, Berlin, 1991.
3. C. Park and R. Snyder, *J. Am. Ceram. Soc.* **78,** 3171 (1995).
4. "Colossal Magnetoresistance, Charge Ordering and Related Properties of Manganese Oxides," (C. N. R. Rao and B. Raveau, Eds.), World Scientific, Singapore, 1998.
5. A. P. Ramirez, *J. Phys. Condes. Matter* **9,** 8171 (1997).
6. C. Michel, M. Hervieu, M. M. Borel, A. Grandin, F. Deslandes, J. Provost, and B. Raveau, *Z. Phys. B* **68,** 421 (1987).
7. M. Maeda, Y. Tanaka, M. Fukutomi, and T. Asano, *Jpn. J. Appl. Phys.* **L27,** 209 (1988).
8. M. A. Subramanian, C. C. Torardi, J. C. Calabrese, J. Goapalkrishnan, K. J. Morrissey, T. R. Askew, R. B. Flippen, U. Chowdhry, and A. W. Sleight, *Science* **2398,** 1015 (1988).
9. J. M. Tarascon, Y. Le Page, P. Barboux, B. G. Bagley, L. H. Greene, W. R. McKinnon, G. W. Hull, M. Giroud, and D. M. Hwang, *Phys. Rev. B* **37,** 9382 (1988).
10. W. R. McKinnon, E. Tselepsis, Y. Le Page, S. P. McAlister, G. Pleizier, J. M. Tarascon, P. F. Miceli, R. Ramesh, G. W. Hull, J. V. Waszczak, J. J. Rhyne, and D. A. Neumann, *Phys. Rev. B* **41,** 4489 (1990).
11. J. Galy, G. Meunier, S. Anderson, and A. Aström, *J. Solid State Chem.* **13,** 142 (1975).
12. H. W. Zandbergen, W. P. Groen, F. C. Mijhoff, G. Van Tendeloo, and S. Amelinckx, *Physica C* **156,** 325 (1988).
13. D. Pelloquin, A. C. Masset, A Maignan, M. Hervieu, C. Michel, and B. Raveau, *J. Solid State Chem.* **148,** 108 (1999).
14. J. Rodriguez-Carvajal, "Collected Abstracts of Powder Diffraction Meeting" (J. Galy, Ed.), p. 127, Toulouse, France, 1990.
15. C. Martin, D. Bourgault, C. Michel, J. Provost, M. Hervieu, and B. Raveau, *Eur. J. Solid State Inorg. Chem.* **26,** 1 (1989).
16. D. Pelloquin, C. Michel, G. van Tendeloo, A. Maignan, M. Hervieu, and B. Raveau, *Physica C* **214,** 87 (1993).
17. A. Urushibara, Y. Moritomo, T. Arima, A. Asamitsu, G. Kido, and Y. Tokura, *Phys. Rev. B* **51,** 14103 (1995).
18. V. Caignaert, B. Domenges, and B. Raveau, *J. Solid State Chem.* **120,** 279 (1995).
19. D. Pelloquin, C. Michel, A. Maignan, M. Hervieu, and B. Raveau, *J. Solid State Chem.* **138,** 278 (1998).
20. J. C. Bouloux, J. L. Soubeyroux, G. Le Flem, and P. Hagenmuller, *J. Solid State Chem.* **38,** 34 (1981).